

Evaluation of RapidScat Ocean Vector Winds for Data Assimilation and Reanalysis

Will McCarty<sup>1</sup>, Mohar Chattopadhyay<sup>2</sup>, Austin Conaty<sup>2</sup>

<sup>1</sup>Global Modeling and Assimilation Office, NASA Goddard Space Flight Center, Greenbelt, MD

<sup>2</sup>Science Systems and Applications, Inc., Lanham, MD

Submitted to Monthly Weather Review

*Draft Submitted 17 Nov 2017 after minor revisions*

Corresponding Author: Will McCarty, Global Modeling and Assimilation Office, NASA Goddard  
Space Flight Center, Greenbelt, MD 20771, USA. E-mail: will.mccarty@nasa.gov

## Abstract

The RapidScat scatterometer was built as a low cost follow-on to the QuikSCAT mission. It flew on the International Space Station (ISS) and provided data from 3 October 2014 to 20 August 2016 and provided surface wind vectors retrieved from surface roughness estimates taken at multiple azimuth angles. These measurements were unique to the historical scatterometer record in that the ISS flies in a low inclination, non-sun-synchronous orbit. Scatterometry-derived wind vectors have been routinely assimilated in both forward processing and reanalysis systems run at the Global Modeling and Assimilation Office (GMAO). As the RapidScat retrievals were made available in near-real-time, they were assimilated in the forward processing system, and the methods to assimilate and evaluate these retrievals are described. Time series of data statistics are presented first for the near-real-time data assimilated in GMAO forward processing. Second, the full data products provided by the RapidScat team are compared passively to the MERRA-2 reanalysis. Both sets of results show that the root mean squared (RMS) difference of the observations and the GMAO model background fields increased over the course of the data record. Furthermore, the observations and the backgrounds are shown to be biased for both the zonal and meridional wind components. The retrievals are shown to have had a net forecast error reduction via the forecast sensitivity observation impact (FSOI) metric, which is a quantification of 24 hour forecast error reduction, though the impact became neutral as the signal to noise ratio of the instrument decreased over its lifespan.

## 1. Introduction

Spaceborne scatterometers provide unique ocean surface wind information globally. However, since scatterometers have historically flown in sun synchronous orbits, there are still temporal data gaps that exist via this sampling strategy. Data assimilation can be used to compensate for the irregularity of the scatterometer record as well as to incorporate conventional observations from ships and buoys, which themselves are irregularly spaced. This results in the generation of global surface wind fields which are regularly spaced both temporally and spatially. The scatterometer-derived ocean vector winds are complementary to the conventional observing network, and the utility of these observations in data assimilation is applicable both in terms of forecasting (Yu and Mcpherson 1984, Atlas et al. 2001, Bi et al. 2011, Liu et al. 2017) and reanalysis (Goswami and Sengupta 2003, Dee et al. 2011a,b).

A scatterometer determines surface roughness from a measured radar backscatter cross section. As surface roughness is a function of near-surface wind speed, a near-surface wind vector can be determined by measuring the same point from multiple azimuth angles. The RapidScat instrument was flown by NASA onboard the International Space Station (ISS, Cooley 2013) as an extension of the NASA scatterometry data record. Scatterometry from space was first demonstrated via the RADSCAT component of the S-193 payload of the Earth Resources Experiment Package on Skylab (Krishen 1975) in the mid-1970s, and follow on missions included the SeaSat-A satellite Scatterometer (Jones et al. 1982), the NASA Scatterometer (NSCAT, Liu et al. 1998), and the SeaWinds instruments onboard QuikSCAT and ADEOS-2 (Wu et al. 1994, Graf et al. 1998). Additionally, ESA (Quilfen and Bentamy 1994),

EUMETSAT (Figa-Saldaña et al. 2002), and ISRO (Kumar et al. 2013) have all flown scatterometers in space.

RapidScat data was made available in near-real-time and was assimilated in the forward processing (FP) system at NASA Goddard Space Flight Center's Global Modeling and Assimilation Office (GMAO). Based on the Goddard Earth Observing System (GEOS) atmospheric data assimilation system (ADAS, Rienecker et al. 2008), this system runs routinely in near-real-time with four six-hour assimilation cycles centered upon 0000, 0600, 1200, and 1800 UTC. Additionally, two medium range forecasts are routinely integrated from the 0000 and 1200 UTC analyses for 10 and 5 days, respectively. GMAO FP is used by a number of NASA science teams and field campaigns for mission and decision support. RapidScat observations were assimilated as near-surface wind vectors, defined by their zonal and meridional components, in FP beginning at 1200 UTC on 12 May 2015.

Also produced at the GMAO is the Modern-Era Retrospective analysis for Research and Applications, Version 2 (MERRA-2, Gelaro et al. 2017) reanalysis. Wind vectors determined via scatterometry were assimilated in the reanalysis. The MERRA-2 scatterometry record begins with the ESA European Remote Sensing (ERS) scatterometer on 5 Aug 1991 and continues through today with the ERS-2, QuikSCAT, and EUMETSAT MetOp Advanced Scatterometer (ASCAT) records (McCarty et al. 2016). RapidScat was not used in MERRA-2 as development had frozen prior to the launch and implementation of the instrument.

The purpose of this study is to summarize the RapidScat mission in the context of GMAO systems in two ways. First, the performance of the RapidScat measurements assimilated in near-real-time in GMAO FP is assessed. Second, multiple data products available from the RapidScat team are considered in comparison to MERRA-2 with the goal of documenting the character of the data in preparation for future reanalyses performed at the GMAO.

## **2. Mission and Data**

RapidScat was launched on 20 September 2014 onboard the SpaceX Commercial Resupply-4 mission and mounted to the Columbus laboratory of the ISS. The ISS orbits at an inclination of  $51.6^\circ$  at a height ranging from 330 to 435 km in a non-sun synchronous orbit. ISS is novel in that it provides scatterometer ocean vector winds in a unique orbit, particularly due to its inclination, compared to traditional earth-observing orbits, most of which are in sun synchronous polar orbits or geostationary orbits. However, earth remote sensing is not its primary objective. This leads to a number of challenges that are fairly unique to these wind retrievals, including the periodic orbit boost maneuvers needed to compensate for drag-induced descents and station attitude maneuvers fundamentally varying the instrument viewing geometry (Cooley 2013).

The instrument is a pencil beam scatterometer operating in the Ku-band at a frequency of 13.4 GHz. The instrument sweeps in a circular motion, measuring the backscatter cross section of the surface at a given point from multiple azimuths. This backscatter cross section is a function of surface roughness, which is highly correlated to wind speed and direction. With multiple

measurements from varying azimuths, the surface roughness can then be used to retrieve a surface wind vector.

RapidScat was a quick and low-cost follow-on to the SeaWinds instrument onboard the QuikSCAT and ADEOS-2 satellites. The instrument was assembled from flight-capable hardware used as test and spare parts from the QuikSCAT mission at the NASA Jet Propulsion Laboratory. A primary change in design required the use of a 0.75 m antenna, a reduction from the 1.0 m antenna used on QuikSCAT. This was necessary to fit launch vehicle and ISS size constraints, though it is noted that the smaller antenna is measuring at approximately half the altitude of the QuikSCAT mission. Due to the similarity to SeaWinds, the ground processing software for QuikSCAT was used with modifications for the ISS implementation (NASA 2016). This includes the wind retrieval algorithm, which is an extension of that used for SeaWinds and is described in Fore et. al (2014).

The instrument provided data from 3 October 2014 to 20 August 2016. Fundamental to the quality of the RapidScat retrievals was a degradation of the instrument's signal to noise ratio (SNR) over the life of the instrument. The instrument team characterized the degradation into five categories: High SNR, which was the nominal operation, and four Low SNR states. These low SNR states were not permanent, as the instrument did shift among the five SNR state. The time periods for these SNR states are shown in Table 1.

### **3. Evaluation of Near-Real-Time Assimilation**

*a. Data and Methodology*

RapidScat data were made available in near-real-time via the RapidScat team. Level 2B surface wind retrievals were acquired via FTP in NetCDF4 format, and the data were acquired with local cutoff of 6 hr 25 min relative to each six hour assimilation cycle. That is, all data made available by JPL at 0625 UTC for the 0000 UTC window, which ranges from 2100 to 0300 UTC, would be transferred from JPL to the GMAO and processed as described in this section. In the event of delayed data processing, the observations would exceed the latency requirements required for the GEOS FP system and would not be considered.

Once acquired from the provider, the data underwent three stages of preprocessing. First, retrievals with a quality flag greater than zero were discarded, constraining the procedure to consider only observations passing all quality checks. These quality checks are described in detail in NASA (2016) and screen the observations that are inadequate for trustworthy retrieval due to a number of factors. These include: inadequate sampling, contamination due to non-liquid water surface types, contamination due to precipitation, and wind speeds that exceed low and high wind speed thresholds of  $3 \text{ ms}^{-1}$  and  $30 \text{ ms}^{-1}$ , respectively. Second, the observations were aggregated to a  $0.5^\circ \times 0.5^\circ$  latitude/longitude grid via averaging in a procedure referred to as superobbing. During this, geolocation was averaged in addition to the zonal and meridional wind components so that the processed locations were weighted towards the raw data locations. This is performed with the aim of producing observations that are more representative of the grid spacing of the analysis procedure. Third, the observations were written as BUFR files following the NCEP Prep format generally used for conventional observation types. In writing the data,

the same data identifiers were used from previous QuikSCAT data as there is no overlap, and thus no conflict.

The preprocessed RapidScat data were assimilated in the GEOS ADAS version 5.13.1. The GEOS ADAS consists of the GEOS atmospheric model (Rienecker et al. 2008, Molod et al. 2015), the Gridpoint Statistical Interpolation (GSI, Wu et al. 2002, Kleist et al. 2009) meteorological assimilation routine, and the Goddard Aerosol Assimilation System (GAAS, Buchard et al. 2016, Randles et al. 2017) aerosol analysis routine. This version was the first 3-dimensional ensemble-variational hybrid (Wang et al. 2013) implementation of the GSI at GMAO. The central forecast model was run on the cubed sphere dynamical core (Putman and Lin 2007) at an approximate resolution  $0.25^\circ \times 0.3125^\circ$  on 72 hybrid-eta levels to 0.01 hPa. The ensemble members used in the hybrid analysis are run using the same model, except at a reduced horizontal resolution of  $1.0^\circ \times 1.25^\circ$ . The GSI analysis is run on a square latitude-longitude grid at a  $0.5^\circ \times 0.625^\circ$  horizontal resolution and the same vertical coordinates as the model. In addition to RapidScat, the system already assimilated ASCAT surface wind vectors, as well as a broad suite of conventional and remotely sensed observations consistent with other global operational numerical weather prediction centers. A description of the global observing system is available in McCarty et al. (2016) for MERRA-2, which is generally consistent with the GEOS GP system during the study period.

Beyond the superobbing performed in preprocessing, the observations were further thinned to a 100 km global thinning mesh within the assimilation system. This thinning was consistent with



the implementation of ASCAT in the GEOS system. Pre-implementation testing found the additional thinning mesh to be slightly beneficial. As the observations are thinned beyond the grid spacing of the analysis procedure, this procedure effectively acts to smooth the information content of the observations. The observations were assimilated with a specified observation error of  $3.5 \text{ ms}^{-1}$  prior to 21 October 2015 and a  $2.5 \text{ ms}^{-1}$  thereafter. This change coincided with a reduction of the specified observation error for a number of different observation types, and was the result of internal testing with the aim of increasing observation weight of the observations in order to correct systematic model biases. The only additional quality control performed was a gross check of the background departure, defined as the difference between the observation and the background field interpolated to the point of the observation. By construction within the GSI, this check is also a function of the observation error – defined as 1.4 times the specified observation error for RapidScat. This value was determined in pre-implementation testing. This parameter was not adjusted when the prescribed RapidScat observation error was changed. As a result, observations with a background departure magnitude greater than  $4.9 (3.5) \text{ ms}^{-1}$  were excluded prior to (after) 21 Oct 2015.

#### *b. Summary of Performance in GMAO Forward Processing*

Routine assimilation of RapidScat observations began with the 1200 UTC assimilation cycle on 6 May 2015 and continued through the 1800 UTC cycle on 19 Aug 2016. The background departure bias and RMS for both wind components, as well as the assimilated observation counts, are shown in Figure 1. The near-real-time data stream, which was sensitive to data downlink delays, resulted in inconsistencies and gaps in the observation counts. The RMS for both components, as well as the assimilated observation counts, change corresponding to the

observation error and gross check change that occurred on 21 Oct 2015. The average assimilated observation count per cycle from 6 May to 20 Oct 2015 was 4714 observations per analysis, but the latency limitations of the data stream caused this count to vary, particularly early in the FP data record. For the period of 15 Jul to 1 Sep 2015, the average assimilated observation count per cycle was 6712, which was more representative of the optimal count for the 6 May to 20 Oct 2015 period. The assimilated background departure RMS for 6 May to 20 Oct 2015 was 1.43 (1.55)  $\text{ms}^{-1}$  for the zonal (meridional) wind components. The mean assimilated background departure over this period for the zonal (meridional) wind was -0.22 (0.15)  $\text{ms}^{-1}$ .

With the observation error and gross check changes, more outlying observations in terms of background departure, were rejected. This resulted in fewer assimilated observations and a reduced RMS. The average assimilated observation count per cycle from 21 Oct 2015 to 19 Aug 2016 was 5326 observations per analysis, and the RMS for the zonal (meridional) wind components for this period was 1.12 (1.21)  $\text{ms}^{-1}$ . The mean background departure over this period for the zonal (meridional) wind was -0.21 (0.05)  $\text{ms}^{-1}$ . Following the data gap from 27 Mar 2016 to 5 Apr 2016, there was an increase in the meridional wind bias that corresponded in a switch from the third to the Low SNR 4 state (Table 1). From the period of 21 Oct 2015 to 26 Mar 2016, the mean meridional wind background departure was 0.01  $\text{ms}^{-1}$ . This mean departure increased to 0.10  $\text{ms}^{-1}$  for the period of 6 Apr 2016 to 19 Aug 2016. For these two periods, the zonal wind remained generally unchanged, with a mean background departure of -0.24  $\text{ms}^{-1}$  for 21 Oct 2015 to 26 Mar 2016 and -0.23  $\text{ms}^{-1}$  for 6 Apr 2016 to 19 Aug 2016.

219 The distribution of the departures in wind speed as a function of the observed wind speed is  
220 shown in Figure 2 for 1-31 June 2015 and 1-31 June 2016. The change in the gross check of the  
221 background departure is apparent between the two time periods, as fewer outliers in background  
222 departure are seen in the 2016 period compared to the 2015 period. The speed background  
223 departure standard deviation is  $1.16 \text{ ms}^{-1}$  ( $1.02 \text{ ms}^{-1}$ ) for the 2015 (2016) period, and the  
224 difference between the two periods is driven by this change in the gross check. There is no clear  
225 signal as a function of wind speed in standard deviation (Fig. 2, dashed red), as they are within  
226 12.9% (8.5%) of the total standard deviation for all wind speeds greater than  $5.0 \text{ ms}^{-1}$  and less  
227 than  $22 \text{ ms}^{-1}$  for the 2015 (2016) periods.

228

229 For both periods, the total background departure bias (Fig. 2, black) is seen to be similar in  
230 magnitude:  $0.69$  and  $0.74 \text{ ms}^{-1}$  for 2015 and 2016, respectively. Both also show that the  
231 magnitude of the bias in background departure, relative to the total bias, increases as a function  
232 of wind speed (Fig. 2, solid red). The difference between the functional and total wind speed  
233 bias exceeds  $1.0 \text{ ms}^{-1}$  at  $18.0 \text{ ms}^{-1}$  and  $21.0 \text{ ms}^{-1}$  for 2015 and 2016, respectively. While for  
234 2015 high wind speed background departure bias is higher, this is due to the fact that the gross  
235 check is larger, thus letting in more outliers that are inherently seen to be skewed positive.

236

237 To further assess the data quality and impact RapidScat had on the GMAO FP system, the  
238 component RMS of all observations, both assimilated and rejected via the gross check, are  
239 shown in Figure 3. In this plot, the component RMS are smoothed and normalized as percent  
240 relative to the mean daily RMS of May 2015. These normalization values are  $1.78$  and  $1.96 \text{ ms}^{-1}$

for the zonal and meridional wind components, respectively. A 60 day raised cosine, or Hann, window is applied to the daily RMS fields of each field as a smoothing operator. All observations are considered for two reasons. First, the elimination of outliers was inconsistent over the assimilation period as the gross check changed on 21 Oct 2015. Second, increase in the variance of the background departures corresponding to a decrease in observation quality would have had a dampened signal by excluding outliers. This inclusion of rejected observations was necessary to directly and consistently assess the observation quality over the entire data record.

The background departure RMS for both wind components were within 3% of the May 2015 levels until 8 Jul 2015. From 8 Jul to 13 Aug 2015, the RMS dropped to a low of 92.7% (91.6%) of the May 2015 levels for the zonal (meridional) components on 3 Aug 2015 (1 Aug 2015). After a data gap from 14 to 29 Aug 2015, the RMS jumped to 104.9% (102.6%) of the May 2015 levels, denoting a change in the observation character (Fig. 3). This gap, and the subsequent increase in RMS, corresponds to the first change from High SNR to the Low SNR 1 state. After peaking in Sept 2015, the RMS stayed within 101-104% (101-105%) of the May 2015 zonal (meridional) RMS until 20 Feb 2016. At this point, an increase in RMS was seen, and From 1 Mar 2016 to the end of the record on 20 Aug 2016, the RMS was within 105-110% (107-110%) of the May 2015 RMS values. The increase in RMS seen from Feb to Apr 2016 corresponds to two changes in SNR state – from Low SNR 2 to Low SNR 3 and from Low SNR 3 to Low SNR 4.

To assess the impact the RapidScat observations had on the analysis, the monthly mean forecast sensitivity observation impact (FSOI, Langland and Baker 2004, Gelaro and Zhu 2009) metric per analysis is also shown in Figure 3. This metric represents a change in 24 hour forecast error due to the each individual observation, where a negative (positive) value quantifies a decrease (increase) in 24 hour forecast error. The forecast error is integrated across variables and quantified using a moist energy norm (Ehrendorfer et al. 1999, Holdaway et al. 2014). The bars in this figure represent the FSOI metric per analysis for all assimilated RapidScat observations, computed daily for the 0000 UTC assimilation cycle, and averaged by month. For the first three months, the FSOI metric indicates a net reduction in 24 forecast error due to the RapidScat observations. Aug 2015 indicates that the RapidScat observations had a net degradation on the 24 hour forecasts, but this was largely driven by one single analysis cycle initialized at 0000 UTC on 11 Aug 2015. For this instance, a numerical instability in the adjoint of the forecast model resulted in unrealistically large values of FSOI for a region off the coast of eastern South Africa. This instability was sampled by 0.3% of the assimilated RapidScat observations and accounted for 56.5% of the total impact for the instrument for this cycle. By excluding this single case, the Aug 2015 value decreases from  $0.002 \text{ J kg}^{-1}$  to  $-9.4 \times 10^{-6} \text{ J kg}^{-1}$ , which is effectively neutral for the month.

Though the RMS increased in Sep 2015, there was no clear change in the FSOI metric between Sep 2015 and Feb 2016. There was also no clear signal seen with the decrease in the observation error on 20 Oct 2015, and more testing would be needed to directly quantify that response in terms of this metric. With the RMS increase in late Feb 2016, the FSOI metric transitioned from a net reduction in forecast error to generally neutral, as its magnitude is reduced to near-zero.

This indicates that the observations were being improperly handled, particularly in that the observation error was reduced at a time when the RMS of the observations indicated a degradation in quality.

To further illustrate the performance of RapidScat for the three periods of stepwise RMS increase, the FSOI per analysis, ranked relative to all other observations, is shown in Figure 4. The three periods shown are for 6 May to 31 Jul 2015, 29 Aug 2015 to 20 Feb 2016, and 1 Mar to 20 Aug 2016. RapidScat is shown to have consistent performance relative to the global observing system during the first two periods, accounting for 0.21% and 0.23% of the total FSOI per analysis. It provided 39% and 44% of the FSOI per analysis of ASCAT, which are the only other scatterometer data assimilated in the GMAO FP system. RapidScat did increase one position in rank, but this was due to the drop of SSMIS in the second period due to the disabling of the instrument on DMSP-F18. The degradation in the FSOI metric in the third period (Fig 3) is also seen in the relative ranking, as the RapidScat FSOI per analysis decreased by 83% from the second period only accounted for 0.04% of the total FSOI per analysis. During this period, RapidScat was the lowest ranking observation class.

#### *c. Case Study – 0600 UTC, 28 May 2015*

To further illustrate the impact of RapidScat in data assimilation, a simple case study is presented. Tropical Depression One-E was first reported from the National Hurricane Center with the 0600 UTC 28 May 2015 *tcvital* observation. Its location is shown in Figure 5. This

307 depression would continue to strengthen, becoming a named tropical cyclone, Andres, with the  
308 1800 UTC *tcvital* report that same day and a hurricane the following day.

309 During this analysis cycle, the environment surrounding the depression was measured in close  
310 proximity by both RapidScat and ASCAT. The assimilated observations – those that pass  
311 quality control - for both scatterometers are shown in Figure 5 (left). ASCAT is shown to  
312 sample only to the east of the storm, while RapidScat samples in all directions of the storm  
313 center. While this is in part fortuitous due to the orbits of each instrument’s observing platform,  
314 the low inclination of the ISS allows for sampling that is largely orthogonal to the ASCAT  
315 measurements, which are measured from highly inclined, sun-synchronous orbits.

316 The analyzed  $p_s$  from an analysis procedure considering all observations except RapidScat is  
317 shown (Fig. 5, left). The analyzed  $p_s$  field and all observations including RapidScat (Fig. 5,  
318 right) is also shown. These two analyses were performed using the same background field,  
319 therefore any differences are explicitly, and only, due to the inclusion or exclusion of the  
320 RapidScat data at this instantaneous time. While the fields are largely similar, it is seen that the  
321 closed secondary low at 12.5°N, 108.75° W is opened by the expansion of the depression  
322 pressure field – specifically illustrated by the 1008 hPa contour. This corresponded to an  
323 increased in curved flow in the wind field of the lowest model level. This is illustrated by  
324 looking at the change in vorticity between both analyses, the difference of which is plotted in  
325 Figure 5 (right). While no RapidScat observations are directly present in the region of increased  
326 vorticity to the northeast of the cyclone center, the horizontal spreading of information from  
327 those observations via the assimilation procedure is shown to adjust the near-surface wind and  
328 surface pressure fields.

These differences were further investigated through forecast integration, though no noted difference in the forecast of the storm from this single instance was seen. Furthermore, a substantial number of case studies would need to be performed to quantify the significance of any perceived difference in forecast quality due to the inclusion of RapidScat data. Pre-implementation experimentation testing the inclusion of RapidScat via standard observing system experiments (OSEs) was performed and showed no significant difference in global forecast and analysis metrics. Both the extension to a significant number of case studies, as well as an assessment of the pre-implementation experimentation, is beyond the scope of this study.

#### **4. Evaluation for Future Reanalysis**

##### *a. Data and Methodology*

For this section, background departures relative to MERRA-2 are considered. These results are all relative to short-term forecasts that served as the background fields in the MERRA-2 reanalysis fields, and the background departures are calculated using the GSI. The resolution of both the background fields and the analysis procedure is  $0.5^{\circ} \times 0.625^{\circ}$  horizontally and the same vertically as the GMAO FP system described in section 3a. By using the GSI, the mapping of the background fields to observation space is consistent with the results shown in the previous section. RapidScat was not assimilated in MERRA-2, and therefore there is no feedback from these data from the background generated from the previous cycle.

Four versions of the Level 2B RapidScat retrievals are available from JPL and are considered in this section. Three versions, which exist for subsets of the data record, are considered as v1.1,



v1.2, and v1.3. Though the entire data record for each version is shown, the data providers state that each version is only valid until the beginning of the subsequent version. The combination of versions is necessary to assemble a data record that covers the full lifespan of the instrument. A fourth version, which is a reprocessing of the entire data record for climate studies, is also considered and referred to as clim\_v1.0. The temporal range of these data streams are given in Table 2.

For the results shown in this system, the same preprocessing methods described in section 3a are used, except no superobbing is performed and no thinning mesh is applied. That is, every observation is considered individually, though the retrieval quality flags are still considered and the data is still converted to BUFR. Furthermore, since the data is simply being compared against MERRA-2, and no assimilation is being performed, the gross error check is not applied.

#### *b. Results*

The mean background departure time series for the four data collections are shown in Figure 6. These means are smoothed using a 60-day Hann window, similar to the results shown in Figure 3. Relative to MERRA-2 background fields, the observations are shown to have a zonal wind bias that increases over the lifespan of the instrument. The mean zonal wind background departures for the four data records is shown in Table 3. In November 2015, there is an increase in the magnitude of the bias in the v1.2 and clim\_v1.0 data. For the clim\_v1.0 data, the zonal mean departure increased in magnitude from  $-0.31 \text{ ms}^{-1}$  for the data record prior to 1 Nov 2015 to  $-0.36 \text{ ms}^{-1}$  for the data record after that date. The v1.1 data did not show the same change in

bias. By the end of the v1.1 data record, these data were not consistent with the other versions, which exhibit more intra-dataset agreement. The meridional wind component shows less bias relative to the MERRA-2 backgrounds than the zonal component. The mean meridional wind background departures of the four data records is shown in Table 3. The meridional component does show a seasonal cycle in the mean departures that is not seen in the zonal component.

The observations show a continual increase in variance, as is illustrated by the background departure RMS shown in Figure 7. Again, a 60-day Hann window is used to filter the statistics. The RMS of the background departure for the zonal and meridional wind components for all four data records are shown in Table 3. For the clim\_v1.0 retrievals, the RMS of the zonal (meridional) component background departure increased by 13.2% (17.5%) from the beginning to the end of the data stream. Specifically, the zonal (meridional) departure RMS was 1.74 (1.94)  $\text{ms}^{-1}$  for the period of 1 Nov 2014 to 31 Jan 2015. It increased to 1.97 (2.28)  $\text{ms}^{-1}$  for the period of 1 June 2016 to 18 Aug 2016. The increasing variances over the time series quantify the degradation of the observing system known to be due to the change in SNR state addressed in Section 2.

The RMS of these data are fundamentally different than the data considered in section 3b. To compare the GMAO FP and clim\_v1.0 data, Figure 8 shows a scatter plot of RapidScat background departure daily RMS for both wind components for matching dates. The mean difference between the zonal GMAO FP daily RMS and the clim\_v1.0 daily RMS was  $-0.03 \text{ ms}^{-1}$ . Due to the increase of outliers in the GMAO FP stream, the median difference

between the two RMS is more representative of the difference and was  $-0.05 \text{ ms}^{-1}$ . For the meridional component, the mean and median daily background departure RMS difference was  $-0.09$  and  $-0.11 \text{ ms}^{-1}$ , respectively. The increase in RMS as a function of time in Figure 8 is consistent with Figure 3 and Figure 7.

There are three key differences to these sets of background departures – particularly in the observations themselves. First, the GMAO FP observations, which were calculated from observations acquired via the RapidScat near-real-time data feed, can be considered the best data available at the time of acquisition. The clim\_v1.0 data was a post-mission reprocessing and is expected to be superior. Second, the near-real-time limitation of the GMAO FP stream can result in low observation counts for a given day, leading to certain daily stats being misrepresentative due to sampling issues. For these two reasons, it is expected that in some cases, the GMAO FP wind component RMS would be larger than the clim\_v1.0 wind components RMS. Third, there was no superobbing performed on the clim\_v1.0 data in this study, while there was superobbing on the GMAO FP observations. Should some component of the observation error be random, the averaging in the superobbing procedure would reduce the variance of that component. For this reason, it would be expected that the GMAO FP RMS would be smaller than the clim\_v1.0 RMS.

## **5. Conclusions and Relevance to Future Reanalyses**

The effort quantified the RapidScat data record as it was used in GMAO forward processing systems and as it could be applied to future reanalyses. Overall, all data records illustrated an

increase in variance, and thus degradation of retrieval quality, over the course of the data record. The cause of these degradations are understood and relate to the signal to noise ratio of the instrument. In terms of forecast impact, the RapidScat data showed, via the FSOI metric, that the observations were acting to reduce the 24 hour forecast error until February 2016. At that point, the change to the Low SNR 3 state corresponded to a change in the FSOI characteristic and a further increase in RMS.

The change in specified observation error used in the assimilation on 21 October 2015 was suboptimal. At the time, there was a decision to fit the data more strongly, though this action was contrary to the subsequent degradation of the data over time. This was illustrated with the increasing RMS over the lifespan of the instrument. It would have been appropriate to increase, rather than reduce, the observation error, but the increase in RMS was difficult to assess in the near-real-time monitoring of GMAO FP. For future reanalysis efforts, the proper approach will be to dynamically prescribe an observation error that aims to keep the ratio of the background departure variance to the prescribed observation error variance near-constant over time. However, additional infrastructure will be needed in the context of the current assimilation system to allow for the dynamic prescription of observation error.

Furthermore, the data was seen to be biased both in a bulk sense as well as a function of wind speed. It would have also been appropriate to screen observations at low and high wind speeds to remove observations that were essentially skewed from the proper normal distribution of background departures. For future reanalyses, more stringent screening based on the observed

wind speed will be implemented. Also, it may be beneficial to perform a bias correction on the observations, as the bias is not consistent with those seen for other scatterometers in MERRA-2 (McCarty et al. 2016). However, the proper implementation of a bias correction procedure for these observations requires more study.

The comparison against MERRA-2 shows that the clim\_v1.0 data record has the best performance in terms of bias and RMS for both wind vector components. In future reanalysis, the use of this data stream, in conjunction with the aforementioned dynamic prescription of observation error, could result in a better use of RapidScat than was performed in GMAO FP.

Perhaps more significant to the future is the effect that ocean vector winds will have on coupled assimilation systems. Historically, near-surface observations have previously been largely constrained by boundary conditions. As ocean-atmosphere model and analysis coupling becomes more direct over time, the observations near the interface will become fundamentally important to how the different earth component models respond to each other. Simplistically, near-surface winds drive ocean surface evaporation, and scatterometry can help better constrain this process and the global water cycle as a result. This also extends into other atmospheric components of an integrated earth system analysis, as the surface winds largely drive sea salt aerosol emissions (Chin et al. 2002). These aerosols have both climatological feedbacks (Ayash et al. 2008, Ma et al. 2008) and can act as cloud condensation nuclei in the marine environment, particularly at high wind speeds (Hudson et al. 2011). This further links the importance of

surface wind observations to the global models as they move towards two-moment  
microphysical schemes (Barahona et al. 2014).

Because of the ongoing development in data assimilation both at the GMAO and throughout the  
community, it is expected that scatterometry will play an increasingly important role. RapidScat  
has the capability of providing a reference between the QuikSCAT, ISRO Oceansat-2  
Scatterometer (OSCAT), and the EUMETSAT Advanced Scatterometer (ASCAT) records with  
its unique orbit. This paper shows that the data contains inconsistencies that should be accounted  
for optimal use of these data in future reanalyses. It also shows, via the FSOI metric, that the  
data did provide benefit to analysis. Ultimately, the RapidScat observations may be of unique  
utility, but only if the nature of the data is well understood and accounted for.

## **Acknowledgments**

The development of the GEOS ADAS, the GMAO FP system, and MERRA-2 were funded by  
NASA's Modeling, Analysis, and Prediction program. Additionally, the implementation of  
RapidScat was performed and funded as part of NASA's contributions to the Joint Center for  
Satellite Data Assimilation. Computational resources were provided by the NASA Center for  
Climate Simulation. This effort benefitted from years of heritage development of the GMAO.  
Explicitly, the authors would like to thank Meta Sienkiewicz, Edmond B. Smith, and Albert  
Huang whose previous developments to the system were directly leveraged in this work.

## 481    **Appendix A**

482    The classes in Figure 4 consist of the following observations:

483	Aircraft	Aircraft-measured temperature and wind
484	AIRS (R)	Atmospheric Infrared Sounder (AIRS) brightness temperatures
485	AMSU-A (R)	Advanced Sounding Microwave Unit-A (AMSU-A) antenna
486		temperatures
487	AMV	Atmospheric Motion Vectors (AMV) derived from GOES,
488		Himawari, and MeteoSat geostationary satellite imagery and
489		MODIS and AVHRR polar-orbiting satellite imagery
490	ASCAT	Ocean vector wind retrievals from the EUMETSAT Advanced
491		Scatterometer (ASCAT)
492	ATMS (R)	Advanced Technology Microwave Sounder (ATMS) antenna
493		temperatures
494	CrIS (R)	Cross-track Infrared Sounder (CrIS) brightness temperatures
495	Dropsonde	Dropsonde-measured temperature, specific humidity, and wind
496	GOES Sounder (R)	Geostationary Operational Environmental Satellite (GOES)
497		Sounder brightness temperatures
498	GPS RO	Global Positioning System Radio Occultation (GPS RO)
499		measurements of bending angle

500	HIRS (R)	High-resolution Infrared Radiation Sounder / 4 (HIRS) brightness
501		temperatures
502	IASI (R)	Infrared Atmospheric Sounding Interferometer (IASI) brightness
503		temperatures
504	Land Surface	Surface observations of pressure, temperature, and wind measured
505		over land
506	Marine Surface	Surface observations of pressure, temperature, specific humidity,
507		and wind measured over water and sea ice
508	MHS (R)	Microwave Humidity Sounder (MHS) antenna temperatures
509	PIBAL	Pilot Weather Balloon (PIBAL) derived winds
510	Radar Winds	Radar-measured winds from NEXRAD and wind profilers
511	RAOB	Rawinsonde-measured surface pressure, temperature, specific
512		humidity, and wind
513	RapidScat	Ocean vector wind retrievals from RapidScat
514	SEVIRI (R)	Spinning Enhanced Visible and Infrared Imager (SEVIRI)
515		brightness temperatures
516	SSMIS (R)	Special Sensor Microwave Imager/Sounder (SSMIS) brightness
517		temperatures
518		
519		



## References

- Atlas, R., and Coauthors, 2001: The Effects of Marine Winds from Scatterometer Data on Weather Analysis and Forecasting. *Bulletin of the American Meteorological Society*, 82, 1965-1990.
- Ayash, T., S. Gong, and C. Q. Jia, 2008: Direct and Indirect Shortwave Radiative Effects of Sea Salt Aerosols. *Journal of Climate*, 21, 3207-3220.
- Barahona, D., and Coauthors, 2014: Development of two-moment cloud microphysics for liquid and ice within the NASA Goddard Earth Observing System Model (GEOS-5). *Geosci. Model Dev.*, 7, 1733-1766.
- Bi, L., J. A. Jung, M. C. Morgan, and J. F. L. Marshall, 2011: Assessment of Assimilating ASCAT Surface Wind Retrievals in the NCEP Global Data Assimilation System. *Monthly Weather Review*, 139, 3405-3421.
- Buchard, V., and Coauthors, 2016: The MERRA-2 Aerosol Reanalysis, 1980-onward, Part II: Evaluation and Case Studies. *Journal of Climate*, submitted.
- Chin, M., and Coauthors, 2002: Tropospheric Aerosol Optical Thickness from the GOCART Model and Comparisons with Satellite and Sun Photometer Measurements. *Journal of the Atmospheric Sciences*, 59, 461-483.
- Cooley, V. M., 2013: Unique Offerings of the ISS as an Earth Observing Platform. 64th International Astronautical Congress conference, Beijing, IAC-13-D19.12.18, JSC-CN-29531

540 Dee, D. P., E. Källén, A. J. Simmons, and L. Haimberger, 2011a: Comments on “Reanalyses  
541 Suitable for Characterizing Long-Term Trends”. *Bulletin of the American Meteorological*  
542 *Society*, 92, 65-70.

543 Dee, D. P., and Coauthors, 2011b: The ERA-Interim reanalysis: configuration and performance  
544 of the data assimilation system. *Quarterly Journal of the Royal Meteorological Society*, 137,  
545 553-597.

546 Ehrendorfer, M., R. M. Errico, and K. D. Raeder, 1999: Singular-Vector Perturbation Growth in  
547 a Primitive Equation Model with Moist Physics. *Journal of the Atmospheric Sciences*, 56,  
548 1627-1648.

549 Figa-Saldaña, J., J. J. W. Wilson, E. Attema, R. Gelsthorpe, M. R. Drinkwater, and A. Stoffelen,  
550 2002: The advanced scatterometer (ASCAT) on the meteorological operational (MetOp)  
551 platform: A follow on for European wind scatterometers. *Canadian Journal of Remote*  
552 *Sensing*, 28, 404-412.

553 Fore, A. G., B. W. Stiles, A. H. Chau, B. A. Williams, R. S. Dunbar, and E. Rodríguez, 2014:  
554 Point-Wise Wind Retrieval and Ambiguity Removal Improvements for the QuikSCAT  
555 Climatological Data Set. *IEEE Transactions on Geoscience and Remote Sensing*, 52, 51-59.

556 Gelaro, R., and Y. Zhu, 2009: Examination of observation impacts derived from observing  
557 system experiments (OSEs) and adjoint models. *Tellus A*, 61, 179-193.

558 Goswami, B. N., and D. Sengupta, 2003: A note on the deficiency of NCEP/NCAR reanalysis  
559 surface winds over the equatorial Indian Ocean. *Journal of Geophysical Research: Oceans*,  
560 108, 21-21 - 21-15.

561 Graf, J. E., T. Wu-yang, and L. Jones, 1998: Overview of QuikSCAT mission-a quick  
562 deployment of a high resolution, wide swath scanning scatterometer for ocean wind  
563 measurement. Southeastcon '98. Proceedings. IEEE, 314-317.

564 Holdaway, D., R. Errico, R. Gelaro, and J. G. Kim, 2014: Inclusion of Linearized Moist Physics  
565 in NASA's Goddard Earth Observing System Data Assimilation Tools. Monthly Weather  
566 Review, 142, 414-433.

567 Hudson, J. G., S. Noble, and V. Jha, 2011: On the relative role of sea salt cloud condensation  
568 nuclei (CCN). Journal of Atmospheric Chemistry, 68, 71-88.

569 Jones, W. L., and Coauthors, 1982: The SEASAT-A satellite scatterometer: The geophysical  
570 evaluation of remotely sensed wind vectors over the ocean. Journal of Geophysical Research:  
571 Oceans, 87, 3297-3317.

572 Kleist, D. T., D. F. Parrish, J. C. Derber, R. Treadon, W.-S. Wu, and S. Lord, 2009: Introduction  
573 of the GSI into the NCEP Global Data Assimilation System. Weather and Forecasting, 24,  
574 1691-1705.

575 Krishen , K., 1975: The significance of the S-193 Skylab experiment using preliminary data  
576 evaluation NASA Technical Report NASA-CR-150989, LEC-4250 76 pp.

577 Kumar, R., A. Chakraborty, A. Parekh, R. Sikhakolli, B. S. Gohil, and A. S. K. Kumar, 2013:  
578 Evaluation of Oceansat-2-Derived Ocean Surface Winds Using Observations From Global  
579 Buoys and Other Scatterometers. IEEE Transactions on Geoscience and Remote Sensing, 51,  
580 2571-2576.

581 Langland, R. H., and N. L. Baker, 2004: Estimation of observation impact using the NRL  
582 atmospheric variational data assimilation adjoint system. *Tellus A: Dynamic Meteorology*  
583 and *Oceanography*, 56, 189-201.

584 Liu, L., K. Garrett, E. Maddy, and S.-A. Boukabara, 2017: Impact Assessment of Assimilating  
585 NASA's RapidScat Surface Wind Retrievals in the NOAA Global Data Assimilation System.  
586 *Monthly Weather Review*, submitted.

587 Liu, W. T., W. Tang, and P. S. Polito, 1998: NASA scatterometer provides global ocean-surface  
588 wind fields with more structures than numerical weather prediction. *Geophysical Research*  
589 *Letters*, 25, 761-764.

590 Ma, X., K. von Salzen, and J. Li, 2008: Modelling sea salt aerosol and its direct and indirect  
591 effects on climate. *Atmos. Chem. Phys.*, 8, 1311-1327.

592 Molod, A., L. Takacs, M. Suarez, and J. Bacmeister, 2015: Development of the GEOS-5  
593 atmospheric general circulation model: evolution from MERRA to MERRA2. *Geosci. Model*  
594 *Dev.*, 8, 1339-1356.

595 NASA, 2016: RapidScat Level 2B NetCDF Guide Document. *Physical Oceanography*  
596 *Distributed Active Archive Center Document CL#16-1418*, 31 pp.

597 Putman, W. M., and S.-J. Lin, 2007: Finite-volume transport on various cubed-sphere grids.  
598 *Journal of Computational Physics*, 227, 55-78.

599 Quilfen, Y., and A. Bentamy, 1994: Calibration/validation of ERS-1 scatterometer precision  
600 products. *Geoscience and Remote Sensing Symposium*, 1994. *IGARSS '94. Surface and*

601       Atmospheric Remote Sensing: Technologies, Data Analysis and Interpretation., International,  
602       945-947 vol.942.

603       Randles, C. A., and Coauthors, 2017: The MERRA-2 Aerosol Reanalysis, 1980 – onward, Part I:  
604       System Description and Data Assimilation Evaluation. Journal of Climate, accepted.

605       Rienecker, M. M., and Coauthors, 2008: The GEOS-5 Data Assimilation System—  
606       Documentation of Versions 5.0.1, 5.1.0, and 5.2.0. Technical Report Series on Global  
607       Modeling and Data Assimilation 27, 109 pp.

608       Wang, X., D. Parrish, D. Kleist, and J. Whitaker, 2013: GSI 3DVar-Based Ensemble–Variational  
609       Hybrid Data Assimilation for NCEP Global Forecast System: Single-Resolution  
610       Experiments. Monthly Weather Review, 141, 4098-4117.

611       Wu, C., and Coauthors, 1994: The SeaWinds scatterometer instrument. Geoscience and Remote  
612       Sensing Symposium, 1994. IGARSS '94. Surface and Atmospheric Remote Sensing:  
613       Technologies, Data Analysis and Interpretation., International, 1511-1515 vol.1513.

614       Wu, W.-S., R. J. Purser, and D. F. Parrish, 2002: Three-Dimensional Variational Analysis with  
615       Spatially Inhomogeneous Covariances. Monthly Weather Review, 130, 2905-2916.

616       Yu, T.-W., and R. D. Mcpherson, 1984: Global Data Assimilation Experiments with  
617       Scatterometer Winds from SEASAT-A. Monthly Weather Review, 112, 368-376.

618

619

620

621

622    **List of Tables**

623    Table 1 – Time periods corresponding to the various signal-to-noise states over the RapidScat  
624    record.

625

626    Table 2 – Temporal range of each RapidScat dataset compared to MERRA-2.

627

628    Table 3 – Mean and RMS of departure between the v1.1, v1.2, v1.3, and clim\_v1.0 observations  
629    and the MERRA-2 background fields for the entirety of each data record.

630

631

632

633

634

635

636

637

638

639

640

Table 1 – Time periods corresponding to the various signal-to-noise states over the RapidScat record.

<b>SNR State</b>	<b>Dates</b>
High SNR	3 Oct 2014 - 15 Aug 2015 18 Sep 2015 - 6 Oct 2015 8 Feb 2016 - 10 Feb 2016
Low SNR 1	19 Aug 2015 - 18 Sep 2015 6 Oct 2015 - 7 Oct 2015 30 Mar 2016 - 31 Mar 2016
Low SNR 2	7 Oct 2015 - 8 Feb 2016 10 Feb 2016 - 11 Feb 2016
Low SNR 3	11 Feb 2016 - 29 Mar 2016 1 Jul 2016 - 2 Jul 2016
Low SNR 4	1 Apr 2016 - 1 Jul 2016 3 Jul 2016 - 20 Aug 2016

Table 2 – Temporal range of each RapidScat dataset compared to MERRA-2.

Version	Dates
v1.1	3 Oct 2014 - 10 Mar 2016
v1.2	19 Aug 2015 - 20 Aug 2016
v1.3	11 Feb 2016 - 20 Aug 2016
clim_v1.0	3 Oct 2014 - 20 Aug 2016



Table 3 – Mean and RMS of departure between the v1.1, v1.2, v1.3, and clim\_v1.0 observations and the MERRA-2 background fields for the entirety of each data record.

Version	MERRA-2 Wind Component Background Departure			
	Mean ( $\text{ms}^{-1}$ )		RMS ( $\text{ms}^{-1}$ )	
	Zonal	Meridional	Zonal	Meridional
v1.1	-0.28	0.04	1.91	2.15
v1.2	-0.34	0.09	2.05	2.32
v1.3	-0.38	0.10	2.06	2.56
clim_v1.0	-0.33	0.00	1.85	2.09

## List of Figures and Captions

Figure 1 – The mean (blue) and RMS (red) of the background departure for assimilated observations for the zonal (top) and meridional (bottom) wind components from the GMAO FP system. Also shown are the assimilated observation counts (gray). The vertical dotted line represents 21 Oct 2015, which corresponds to the change of the specified observation error and gross check magnitude described in section 3a.

Figure 2 – Distribution of the wind speed background departure as a function of the observed wind speed for 1-31 June 2015 (left) and 1-31 June 2016 (right). Also shown is the background departure mean of all wind speeds (black dashed), the background departure mean as a function of wind speed (red solid), and the standard deviation, plus or minus the speed dependent mean, as a function of wind speed (red dashed).

Figure 3 – The monthly mean FSOI per analysis (green) and the smoothed relative zonal (red) and meridional (blue) wind background departure RMS from GMAO FP. The daily zonal and meridional wind RMS are normalized as a percent of the May 2015 mean daily RMS – 1.78 and 1.96 ms<sup>-1</sup>, respectively – and are smoothed using a 60 day Hann smoother. Gaps in the RMS curves correspond to periods with missing data, consistent with Figure 1.

Figure 4 – Ranking of observation classes by the mean FSOI per analysis for the given periods. The observation classes are shaded relative to their FSOI per analysis. Observation classes are

connected from period to period by gray lines, with the exception of RapidScat, which is connected by red lines. Radiance observations are denoted by (R). Observation classes are described in Appendix A.

Figure 5 – The surface pressure analyses for 0600 UTC 28 May 2015 for all observations excluding RapidScat (left, black contour) and all observations including RapidScat (right, black contours) are shown and contoured every 2 hPa. The location, direction, and speed of observations passing all quality control procedures for RapidScat (left, green barbs) and ASCAT (left, black barbs) are shown. The positive (right, solid green contours) and negative difference (right, dashed green contours) in lowest model level vorticity between the two analyses is contoured every  $1 \times 10^{-5} \text{ s}^{-1}$ . Positive (negative) vorticity differences indicate that the inclusion of RapidScat has increased (decreased) the vorticity at the lowest model level. The black circle denotes the location of the storm as reported by the National Hurricane Center at this time.

Figure 6 – The daily background departure mean relative to MERRA-2 of the zonal (top) and meridional (bottom) winds for the v1.1 (green), v1.2 (red), v1.3 (blue), and clim\_v1.0 (black) datasets. The values are smoothed using a 60 day Hann window.

735 Figure 7 - The daily background departure RMS relative to MERRA-2 of the zonal (top) and  
736 meridional (bottom) winds for the v1.1 (green), v1.2 (red), v1.3 (blue), and clim\_v1.0 (black)  
737 datasets. The values are smoothed using a 60 day Hann window.

738

739 Figure 8 – Scatterplot of the matched daily background departure RMS for the zonal (left) and  
740 meridional (right) wind components for those assimilated in GMAO FP and the clim\_v1.0  
741 calculated relative to MERRA-2. The points of the scatterplot are shaded by analysis date.

742

743

744

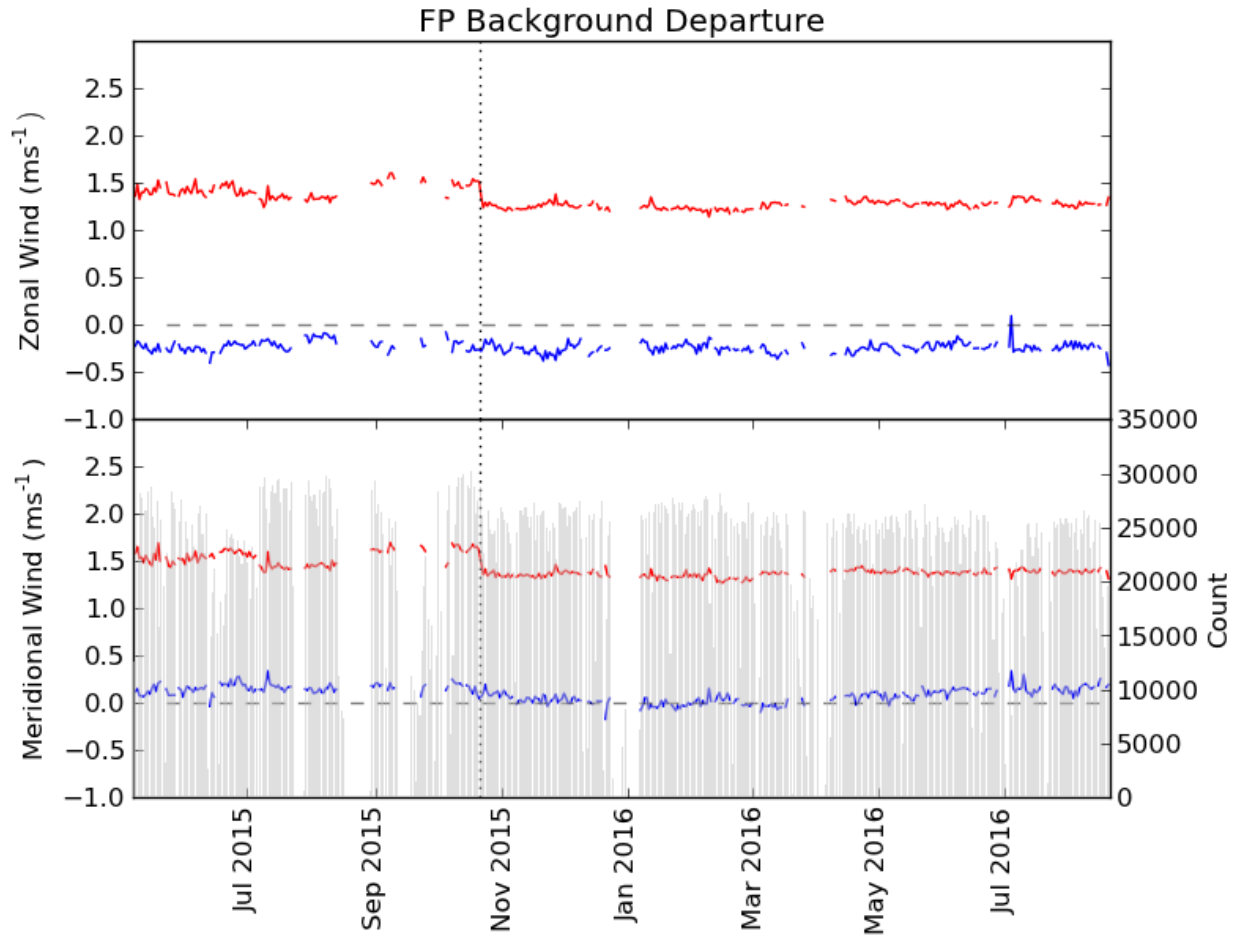


Figure 1 – The mean (blue) and RMS (red) of the background departure for assimilated observations for the zonal (top) and meridional (bottom) wind components from the GMAO FP system. Also shown are the assimilated observation counts (gray). The vertical dotted line represents 21 Oct 2015, which corresponds to the change of the specified observation error and gross check magnitude described in section 3a.

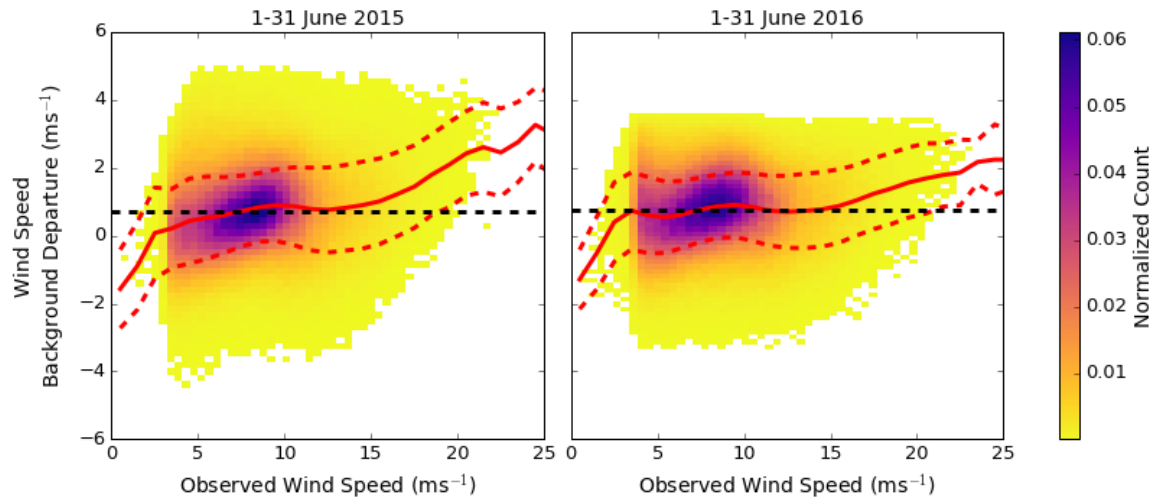


Figure 2 – Distribution of the wind speed background departure as a function of the observed wind speed for 1-31 June 2015 (left) and 1-31 June 2016 (right). Also shown is the background departure mean of all wind speeds (black dashed), the background departure mean as a function of wind speed (red solid), and the standard deviation, plus or minus the speed dependent mean, as a function of wind speed (red dashed).

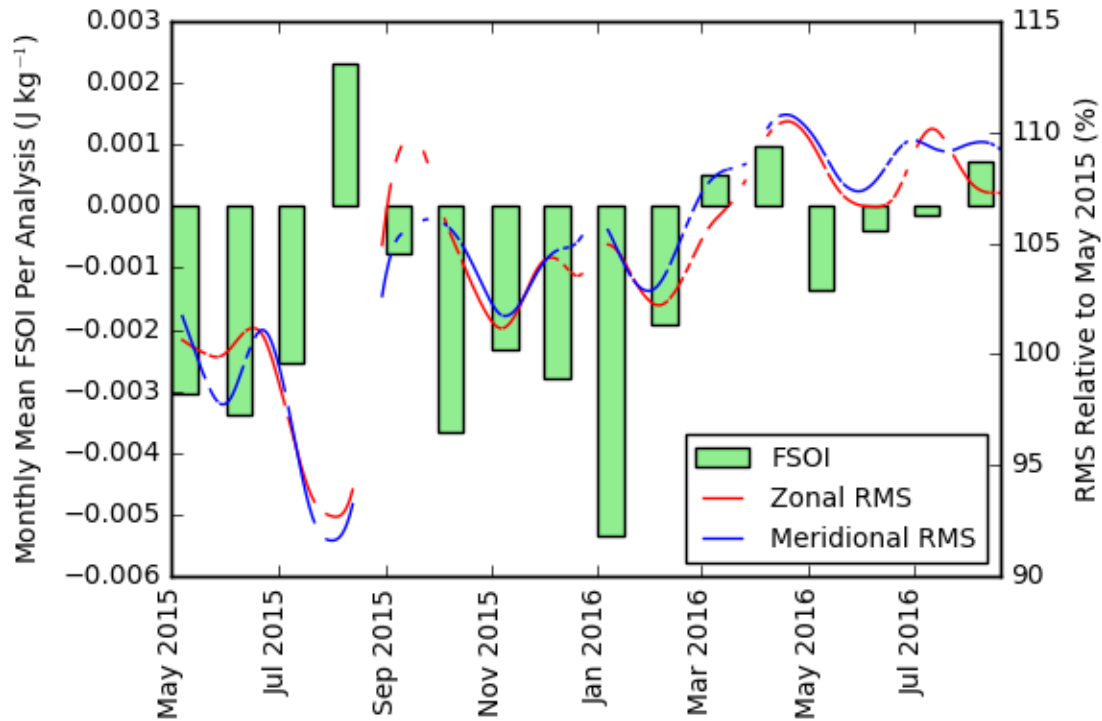


Figure 3 – The monthly mean FSOI per analysis (green) and the smoothed relative zonal (red) and meridional (blue) wind background departure RMS from GMAO FP. The daily zonal and meridional wind RMS are normalized as a percent of the May 2015 mean daily RMS – 1.78 and 1.96  $\text{ms}^{-1}$ , respectively – and are smoothed using a 60 day Hann smoother. Gaps in the RMS curves correspond to periods with missing data, consistent with Figure 1.

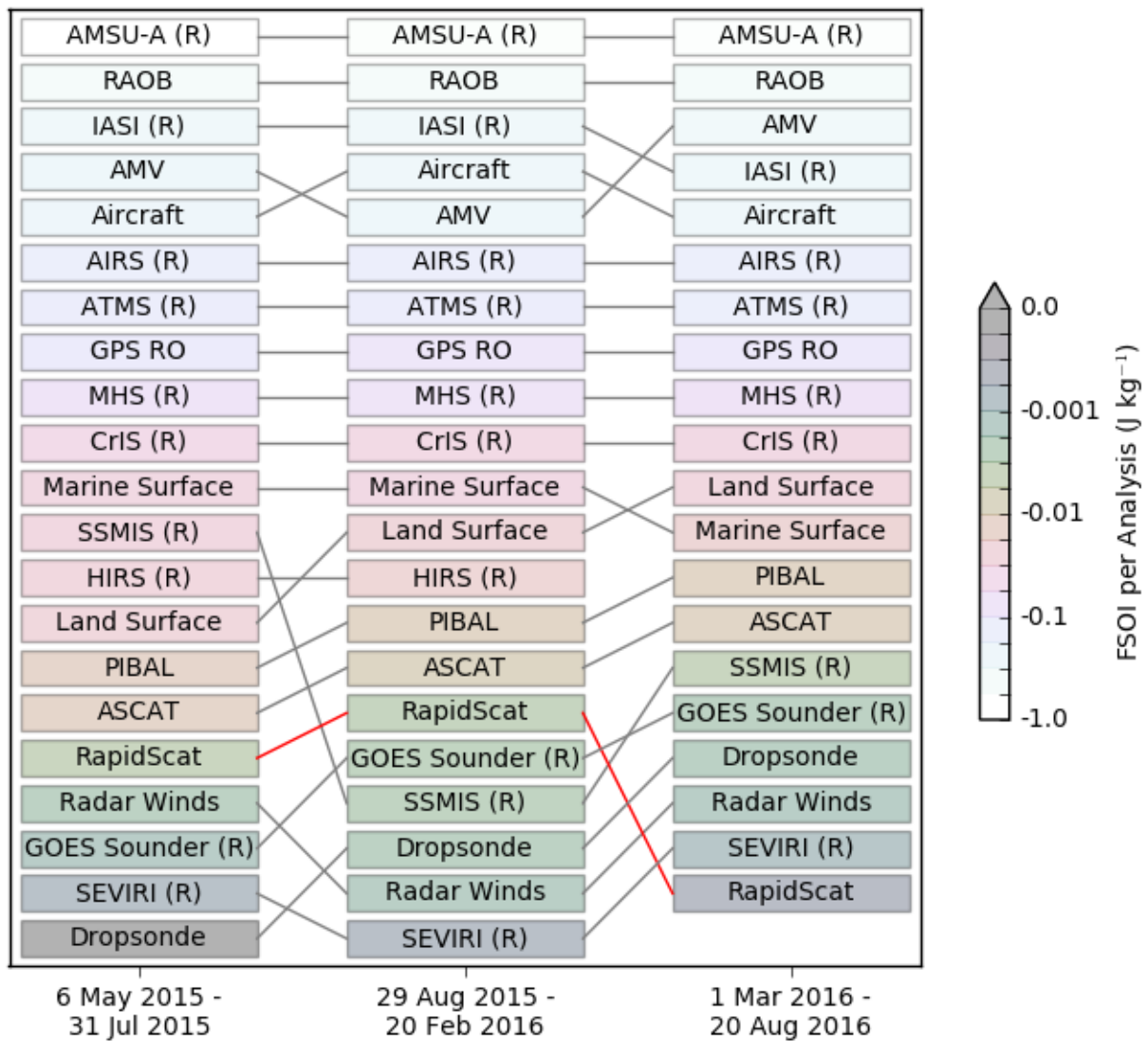


Figure 4 – Ranking of observation classes by the mean FSOI per analysis for the given periods.

The observation classes are shaded relative to their FSOI per analysis. Observation classes are connected from period to period by gray lines, with the exception of RapidScat, which is connected by red lines. Radiance observations are denoted by (R). Observation classes are described in Appendix A.



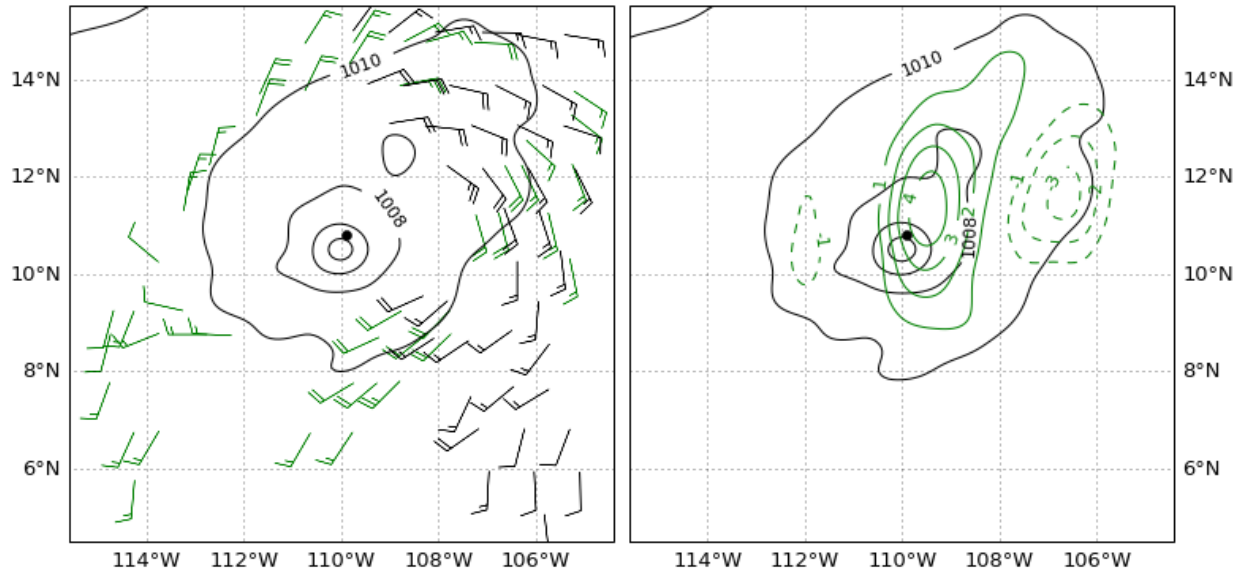


Figure 5 – The surface pressure analyses for 0600 UTC 28 May 2015 for all observations excluding RapidScat (left, black contour) and all observations including RapidScat (right, black contours) are shown and contoured every 2 hPa. The location, direction, and speed of observations passing all quality control procedures for RapidScat (left, green barbs) and ASCAT (left, black barbs) are shown. The positive (right, solid green contours) and negative difference (right, dashed green contours) in lowest model level vorticity between the two analyses is contoured every  $1 \times 10^{-5} \text{ s}^{-1}$ . Positive (negative) vorticity differences indicate that the inclusion of RapidScat has increased (decreased) the vorticity at the lowest model level. The black circle denotes the location of the storm as reported by the National Hurricane Center at this time.

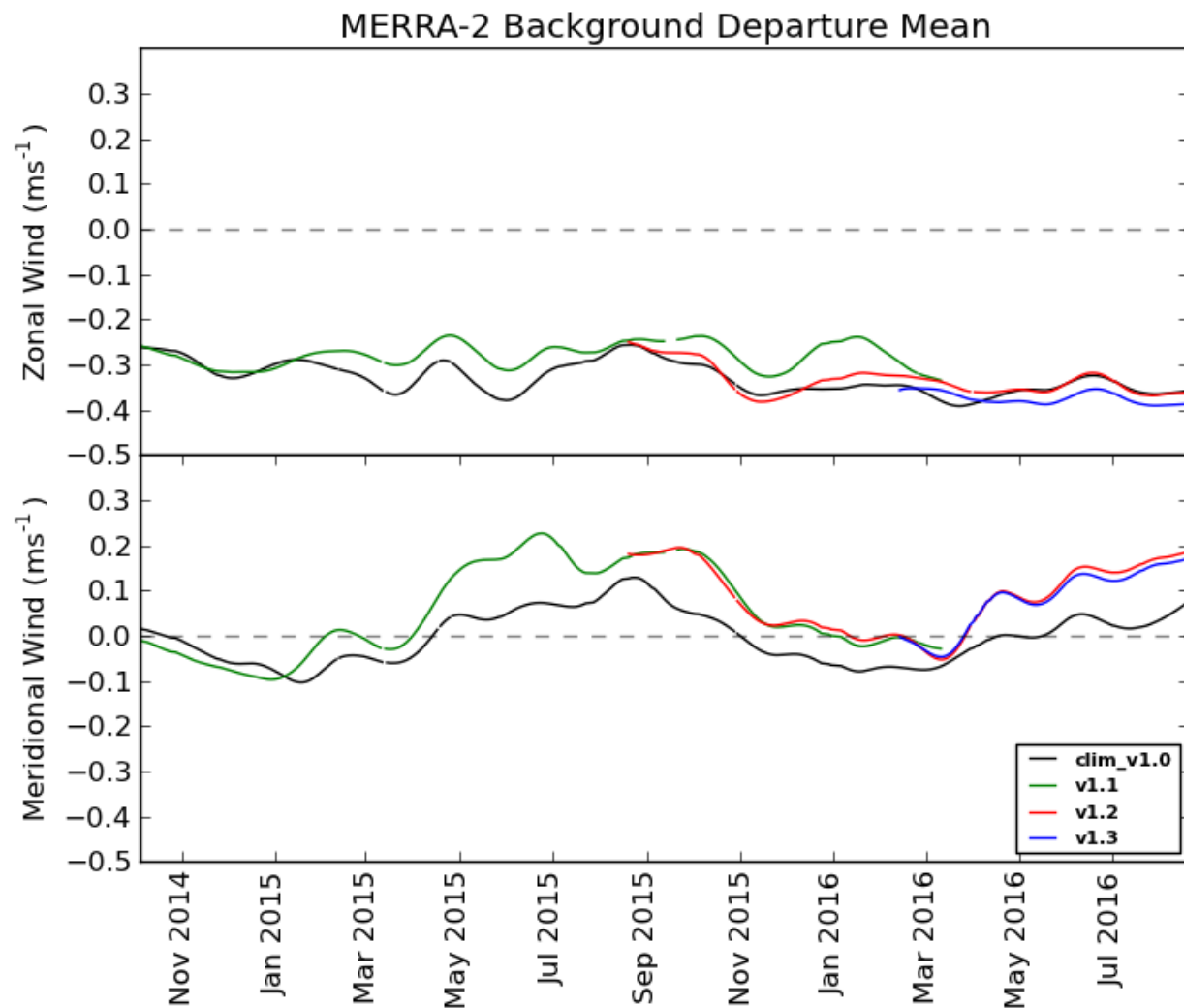


Figure 6 – The daily background departure mean relative to MERRA-2 of the zonal (top) and meridional (bottom) winds for the v1.1 (green), v1.2 (red), v1.3 (blue), and clim\_v1.0 (black) datasets. The values are smoothed using a 60 day Hann window.

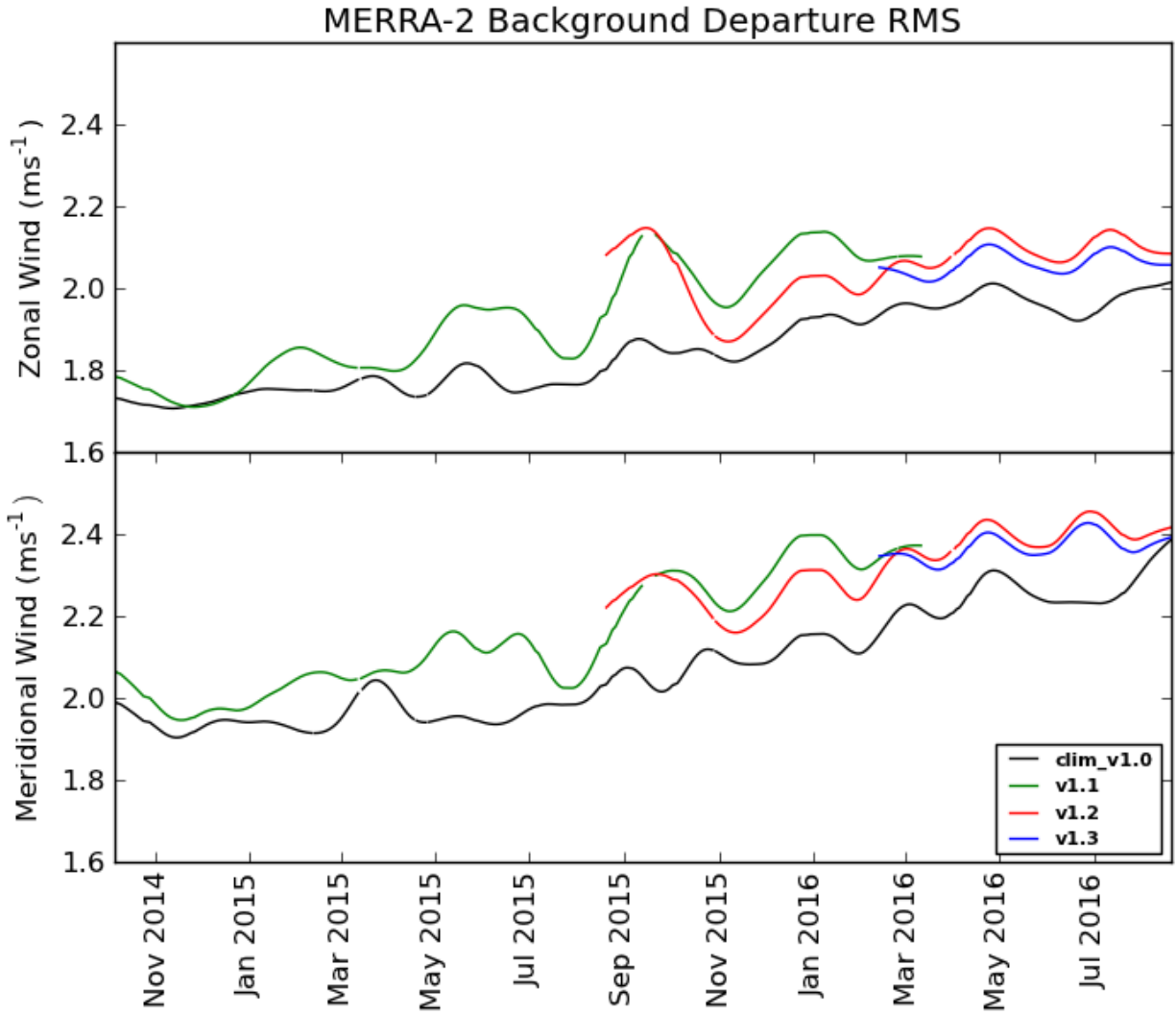


Figure 7 - The daily background departure RMS relative to MERRA-2 of the zonal (top) and meridional (bottom) winds for the v1.1 (green), v1.2 (red), v1.3 (blue), and clim\_v1.0 (black) datasets. The values are smoothed using a 60 day Hann window.

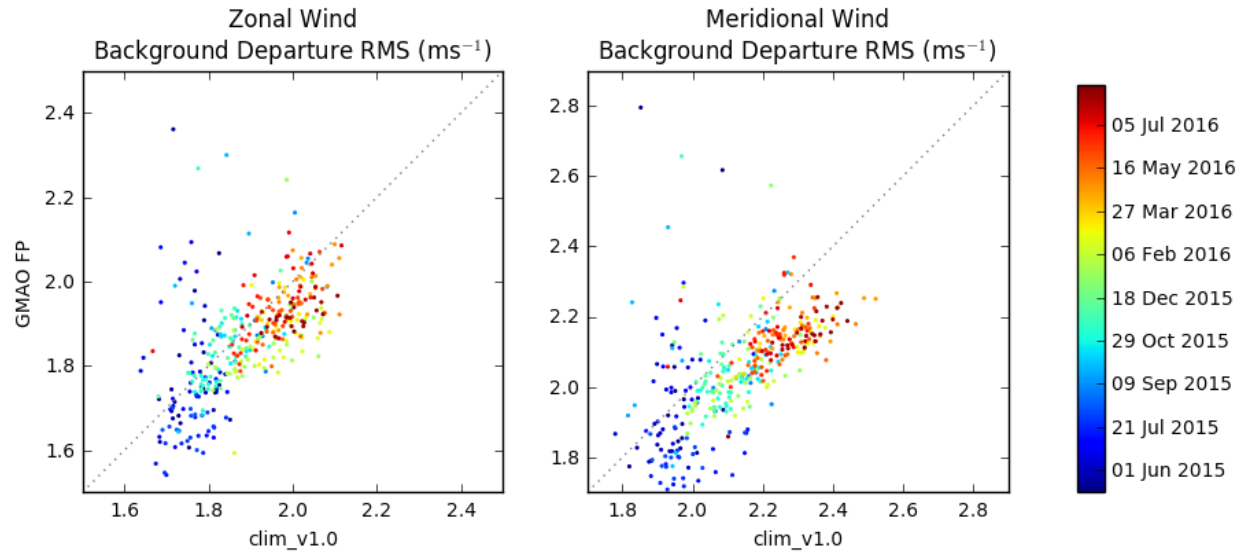


Figure 8 – Scatterplot of the matched daily background departure RMS for the zonal (left) and meridional (right) wind components for those assimilated in GMAO FP and the clim\_v1.0 calculated relative to MERRA-2. The points of the scatterplot are shaded by analysis date.